scientific reports

Check for updates

OPEN

ZrO_2 supported Fe-based catalysts for direct synthesis of light olefins via CO_2 hydrogenation

Elka Kraleva[1]✉, Maria Luisa Saladino[2,4], Cristina Giordano[3], Rosina Celeste Ponterio[4] & Udo Armbruster[1]

The catalytic hydrogenation of carbon dioxide (CO_2) to light olefins provides a sustainable route for producing key chemical intermediates and reducing dependence on fossil-based feedstocks. In this study, FeK, FeCoK, and FeCuK catalysts supported on ZrO_2 were synthesized by a simple wet impregnation method and evaluated for CO_2 hydrogenation. The goal of the study was to understand how secondary metal promoters (Co or Cu) influence the structural and electronic properties of K-promoted Fe/ZrO_2 catalysts and how these modifications affect CO_2 conversion and product selectivity. Among the catalysts tested, FeCoK/ZrO_2 showed the highest performance, achieving around 40% CO_2 conversion and 30% light-olefin selectivity, compared with 40% conversion and 22% selectivity for FeCuK/ZrO_2 under identical conditions (400 °C, 3 MPa, H_2/CO_2 = 3). The FeCuK catalyst exhibited higher CO yield, suggesting enhanced reverse water–gas shift (RWGS) activity, while Co promotion facilitated the formation and stabilization of iron carbides, improving chain growth and olefin selectivity. These findings demonstrate that the addition of Co or Cu effectively tunes the competition among RWGS, methanation, and hydrocarbon chain-growth pathways. Furthermore, the simple impregnation method yielded catalytic behavior comparable to more complex synthesis approaches, highlighting its potential scalability for CO_2-to-olefin conversion.

Keywords CO_2 hydrogenation, Light olefin, Iron-potassium catalysts, ZrO_2 support

The growing global demand for light olefins (C_2–C_4), key feedstocks for the production of polymers, solvents, and fuels, continues to rise, with the global market expected to exceed USD 475 billion by 2027[1]. Traditionally, olefins are produced through energy-intensive petrochemical routes such as steam cracking and methanol-to-olefins (MTO) processes, which rely heavily on fossil resources. In this context, the conversion of carbon dioxide (CO_2) with green hydrogen (H_2) into value-added hydrocarbons offers a promising alternative for achieving carbon-neutral chemical production[2–4]. However, direct CO_2 hydrogenation faces several challenges, including the low thermodynamic driving force for CO_2 activation, competing side reactions such as the reverse water–gas shift (RWGS) and methanation, and the need for catalysts that can simultaneously achieve high CO_2 conversion, high light-olefin selectivity, and excellent stability[5,6].

Among transition metals, iron (Fe) and cobalt (Co) have emerged as benchmark catalysts for Fischer–Tropsch synthesis (FTS) and CO_2 hydrogenation due to their ability to activate CO and H_2 and facilitate C–C bond formation[7–12]. Fe-based catalysts exhibit bifunctional behavior: Fe_3O_4 drives the RWGS reaction, while metallic Fe and iron carbides (Fe_5C_2, Fe_2C) catalyse hydrocarbon chain growth[13–15]. Despite their versatility, Fe catalysts often suffer from deactivation through oxidation or carbon deposition and exhibit limited selectivity toward light olefins. Conversely, Co catalysts display high hydrogenation activity but mainly produce methane[2,16]. Therefore, rational catalyst modification through promoters and supports is essential to tune the product distribution toward desired C_2–C_4 olefins.

The incorporation of alkali metals, transition-metal promoters, and oxide supports can markedly alter the catalytic behavior of Fe-based systems. Potassium (K) is known to serve as an electronic promoter that increases CO_2 adsorption and suppresses H_2 dissociation, thereby enhancing CO formation and C–C coupling[17–20]. It enriches the electron density of Fe sites, stabilizing iron carbides and increasing olefin/paraffin ratios. Cobalt

[1]Leibniz Institute for Catalysis, Albert-Einstein-Str. 29A, 18059 Rostock, Germany. [2]Department of Biological, Chemical and Pharmaceutical Sciences and Technologies (STEBICEF)-University of Palermo, Viale delle Scienze, Bld.17, Palermo I-90128, Italy. [3]School of Physical and Chemical Sciences, Queen Mary University of London, Mile End Road, London E1 4NS, UK. [4]Institute for Chemical and Physical Processes IPCF-Messina, CNR, Viale Ferdinando Stagno d'Alcontres 37, Messina I-98158, Italy. ✉email: elka.kraleva@catalysis.de

(Co) addition to Fe introduces a Fe–Co synergy that enhances hydrogenation kinetics and favors the formation of active Fe–Co alloy or interface species, promoting light-olefin formation while maintaining Fe's chain growth ability[21–23]. In contrast, copper (Cu) functions primarily as a structural and electronic promoter that facilitates Fe reduction, enhances CO formation via the RWGS reaction, and suppresses excessive methanation[11,24–26]. These promoters induced modifications lead to distinct electronic and structural properties that can be systematically compared using FeK, FeCoK, and FeCuK catalysts.

Support materials such as SiO_2, Al_2O_3, TiO_2, and ZrO_2 have previously been examined for CO_2-FT synthesis[15,17,18,22,23,27,28]. The ZrO_2 support plays a crucial role in the catalytic performance of FeK catalysts for FTS. ZrO_2 exhibits high thermal stability, tunable surface acid–base properties, and the ability to form oxygen vacancies that enhance CO_2 activation[29,30]. Furthermore, ZrO_2 supports facilitate strong metal–support interactions, which improve metal dispersion, stabilize Fe-carbide species, and promote electron transfer at the Fe–ZrO_2 interface[31]. Studies have also demonstrated that monoclinic ZrO_2 (m-ZrO_2) promotes CO_2 hydrogenation by providing active oxygen vacancies and improving water desorption, which mitigates oxidation of active Fe phases[12,29,31,32].

Building upon these insights, this study focuses on a systematic comparison of FeK, FeCoK, and FeCuK catalysts supported on ZrO_2. The rationale for selecting these specific compositions is twofold. First, it enables the investigation of how alkali (K) and transition-metal (Co, Cu) promoters influence the structure–activity relationship of Fe-based catalysts in CO_2 hydrogenation. Second, it allows for the isolation of synergistic effects among the active metals and the ZrO_2 support under controlled loadings, facilitating a clear mechanistic understanding. The chosen Fe, Co, Cu, and K loadings are based on prior optimization studies that balance activity, selectivity, and stability[33–35]. Fixed metal ratios also enable direct comparison of the effects of Co and Cu addition, as recommended by recent literature.

The present work aims to elucidate how different promoter combinations (K, Co, Cu) and their interactions with ZrO_2 influence CO_2 hydrogenation pathways, particularly the balance between RWGS, methanation, and chain growth reactions. To investigate the effect of incorporating Co or Cu into K-promoted Fe/ZrO_2 catalysts (FeCoK/ZrO_2 and FeCuK/ZrO_2) and to evaluate the advantages of this optimized composition and metal loading, a simple wet impregnation procedure was employed, in contrast to more complex methods such as co-precipitation or sol–gel synthesis. This approach offers several benefits, including reduced synthesis time, lower energy and chemical consumption, improved reproducibility, and easier scalability for potential industrial application. Based on literature reports, the selected formulation, comprising 10 wt% Fe, M/(Fe + M) = 0.17, and 1.3 wt% K, represents an optimal ratio that ensures good metal dispersion, enhanced reducibility, and favorable catalytic performance in CO_2 conversion and related hydrogenation reactions[12,36]. By combining structural characterization and catalytic performance evaluation, this study provides fundamental insights into the design of multi-promoted Fe-based catalysts with enhanced selectivity toward light olefins.

Results and discussion

Structure, morphology and reducibility of samples– SBET, XRD, TEM, TPR

The N_2 adsorption–desorption isotherms of ZrO_2 and metal-loaded samples (Fig. 1) exhibit type IV isotherms with H_3-type hysteresis loops, characteristic of mesoporous structures with slit-like pores. The absence of a steep uptake at low relative pressures ($p/p_0 < 0.2$) indicates negligible microporosity, while the sharp increase at high p/p_0 (> 0.8) reflects capillary condensation in secondary voids between ZrO_2 particles. The corresponding BJH pore-size distributions show a narrow peak centered at approximately 12 nm. Given that the materials were prepared by impregnation and calcination without any templating, these features are attributed to interparticle voids rather than ordered mesopores within the zirconia crystallites. The commercial monoclinic ZrO_2 (m-ZrO_2) purchased from DK-Japan was used as catalyst support. This material inherently exhibits a mesoporous-like structure, which we confirmed through N_2 adsorption–desorption (SBET) analysis.

The textural parameters summarized in Table 1 reveal that incorporation of Fe and Fe–Co species led to a moderate decrease in surface area and pore volume (from 106.3 $m^2\ g^{-1}$ and 0.32 $cm^3\ g^{-1}$ for ZrO_2 to 78.9 $m^2\ g^{-1}$ and 0.24 $cm^3\ g^{-1}$ for FeK/ZrO_2, and 86.3 $m^2\ g^{-1}$ and 0.26 $cm^3\ g^{-1}$ for FeCoK/ZrO_2), indicating partial blockage of the mesopores by metal oxides. In contrast, FeCuK/ZrO_2 shows a pronounced decrease in surface area (26.5 $m^2\ g^{-1}$) and pore volume (0.11 $cm^3\ g^{-1}$), accompanied by an increase in average pore diameter (16.3 nm). This suggests that the incorporation of Cu caused partial pore coalescence or sintering of the support during thermal

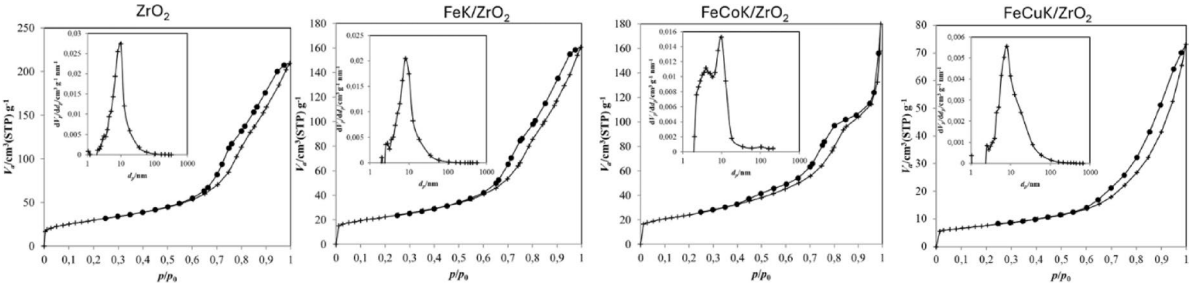

Fig. 1. N_2 adsorption–desorption isotherms and corresponding pore size distribution curves of ZrO_2, FeK/ZrO_2, FeCoK/ZrO_2, and FeCuK/ZrO_2.

Samples	Surface area	Total pore volume	Average pore diameter	CSR* size (nm)	
	(m2g-1)	(cm3 g-1)	(nm)	Scherrer analysis	
ZrO_2	106,3	0,32	12,03	14	
FeK/ZrO_2	78,9	0,24	12,34	12,7	25
$FeCoK/ZrO_2$	86,34	0,26	11,89	8	23
$FeCuK/ZrO_2$	26,5	0,1079	16,29	7,9	29
CSR* Crystallite size calculated using the Scherrer equation					

Table 1. Textural properties of samples.

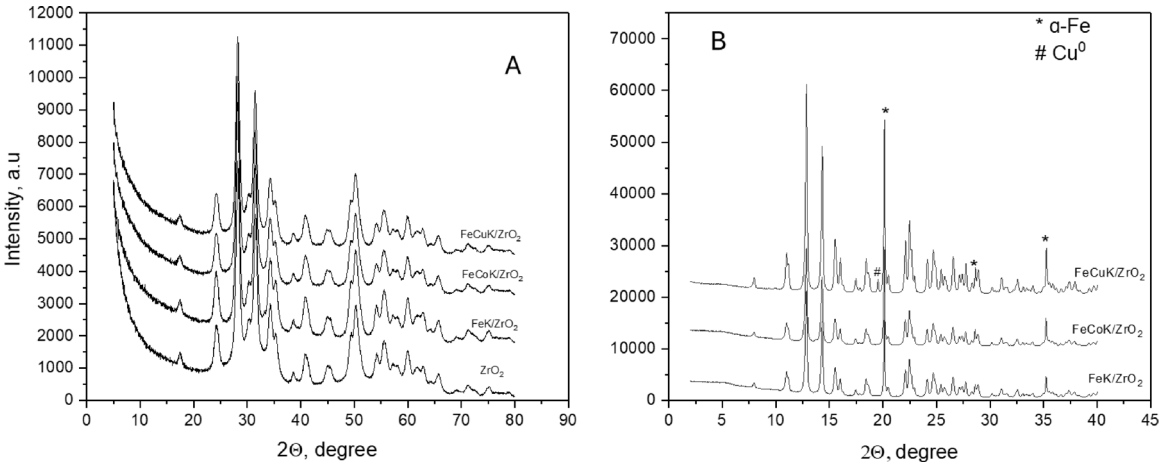

Fig. 2. XRD patterns of ZrO2, FeK/ZrO2, FeCoK/ZrO2 and FeCuK/ZrO2 samples. **A**: calcined samples were recorded using Cu Kα radiation and **B**: after reduction, using Mo Kα radiation (λ = 0.07093 nm).

treatment, leading to structural densification and loss of mesoporosity. Despite these changes, all samples retain mesoporous characteristics, confirming that the overall pore framework of ZrO_2 remains preserved after metal loading.

X-ray diffraction (XRD) patterns of the calcined samples, presented in Fig. 2A, were recorded using Cu Kα radiation, while measurements of the reduced samples, Fig. 2(B), were performed using Mo Kα radiation (λ = 0.07093 nm) to minimize fluorescence effects from metallic Fe species and to improve the overall signal-to-noise ratio. The XRD patterns of the ZrO_2-based catalysts (Fig. 2A) exhibit characteristic reflections of monoclinic ZrO_2 (JCPDS No. 37–1484)[33], confirming that the crystalline structure of the support remains intact after metal loading. No additional diffraction peaks associated with Fe, Co, or Cu oxides were observed, suggesting that the active metal species are highly dispersed or amorphous. Compared with the bare ZrO_2, the FeK/ZrO_2 and $FeCoK/ZrO_2$ samples show slightly broadened peaks, indicative of reduced crystallite size or increased lattice strain induced by metal incorporation. In contrast, the $FeCuK/ZrO_2$ sample displays somewhat sharper diffraction peaks, implying that Cu promotes partial sintering or crystallite growth of ZrO_2 during calcination, consistent with the substantial loss of surface area observed in the N_2 physisorption results. Overall, the XRD and BET analyses collectively indicate that Fe and Co are well dispersed on ZrO_2, while Cu loading significantly alters the textural and structural properties of the support.

XRD analysis of the reduced catalysts, presented in Fig. 2B (measured with a Mo detector) shows that α-Fe is the predominant crystalline phase in all samples, indicating successful reduction of iron. This is expected, since under the applied reduction conditions (400 °C in H_2 flow) Fe_2O_3 should be completely reduced to metallic Fe, regardless of the promoter used. Using Mo Kα radiation, the XRD patterns of the reduced samples show the characteristic reflections of ZrO_2 within the examined 2θ range. No additional or shifted ZrO_2 reflections were detected after reduction, indicating that the phase composition of the support (monoclinic/tetragonal ZrO_2) remains unchanged under the applied conditions.

The observed ZrO_2 peaks are consistent with the expected support structure, and no new ZrO_2-related phases or reconstruction-induced reflections were identified.

FeK/ZrO_2 exhibits only α-Fe and m-ZrO_2 peaks, suggesting that potassium acts as an electronic promoter without forming separate crystalline phases. Incorporation of Co in $FeCoK/ZrO_2$ leads to slightly broader α-Fe peaks, indicative of smaller Fe crystallites or higher dispersion, while no distinct Co^0 peaks are observed, consistent with Co being highly dispersed or forming a solid solution with Fe. Parallel with m-ZrO2 peak also t-ZrO2 was indict. In $FeCuK/ZrO_2$, metallic Cu peaks are clearly visible, confirming the presence of Cu^0 and

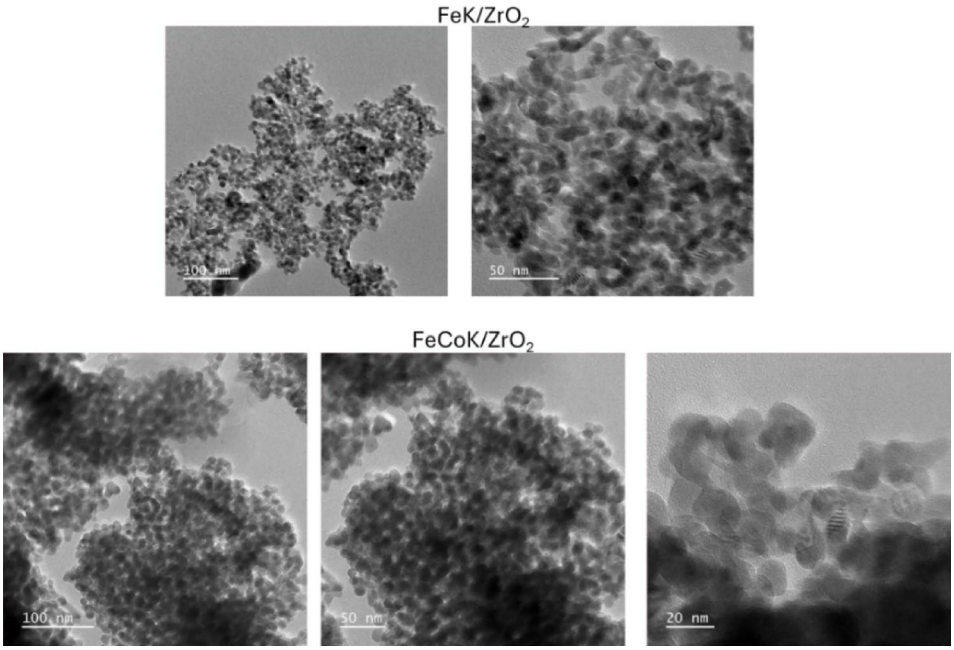

Fig. 3. TEM micrographs at different magnification of FeK/ZrO_2, and $FeCoK/ZrO_2$ samples.

Sample Name	Amount of H2 theoretically [µmol/g]	Amount of H2 experimentally [µmol/g]
$FeCuK/ZrO_2$	3055.4	2804.2
FeK/ZrO_2	2688.2	1025
$FeCoK/ZrO_2$	3239	1381

Table 2. The theoretical and experimentally hydrogen consumption for the samples.

its role in enhancing Fe reducibility, likely via hydrogen spillover. Peak broadening trends suggest smaller Fe crystallites in the Co-promoted sample, whereas sharp Cu peaks point to well-crystallized Cu particles. No significant ZrO_2 reflections are detected in the 2θ range examined, indicating a mostly weakly crystalline support, mainly in monoclinic form. Overall, the diffractograms confirm effective reduction of the active metals and highlight the influence of promoters on particle size, dispersion, and crystallinity.

The TEM micrographs of promoted FeK/ZrO_2 and $FeCoK/ZrO_2$ catalysts exhibited very similar images (Fig. 3) which revealed that both catalysts have similar morphology, i.e., spherical polycrystalline nanoparticles. Mainly iron nanoparticles of 20 nm mean diameter were homogeneously dispersed in the ZrO_2 matrix. Local agglomeration of Fe nanoparticles was also observed whereas the promoters Co and K appear to be homogeneously distributed as very small particles.

The reducibility of the catalysts was evaluated by H_2 temperature-programmed reduction (H_2-TPR), and the results are summarized in Table 2; Fig. 4. Measurements were performed using a thermal conductivity detector (TCD), calibrated with a CuO standard to enable semi-quantitative comparison of H_2 consumption among the catalysts.

The FeK/ZrO_2 catalyst exhibits a main reduction peak centered at approximately 500 °C with a shoulder near 350 °C, corresponding to the stepwise reduction of $Fe_2O_3 \rightarrow Fe_3O_4 \rightarrow Fe^0$[13]. The broad main peak indicates the coexistence of Fe species with different reducibility, likely arising from Fe–O–Zr interactions at the metal–support interface.

The $FeCoK/ZrO_2$ catalyst displays a similar profile, with a slightly shifted main peak at ~ 510 °C and weak shoulders at ~ 350 °C and ~ 480 °C. These features correspond to the reduction of bulk Fe_2O_3, surface Fe–Co oxide phases, and small Fe particles with varying interactions with ZrO_2[34–37]. The broader profile compared with FeK/ZrO_2 suggests a more heterogeneous distribution of reducible species, possibly due to mixed oxide formation and increased oxygen vacancy concentration. However, Co does not significantly enhance overall Fe reducibility, as reflected in the lower H_2 uptake (~ 42.6% of theoretical). The total H_2 consumption indicates that approximately 42.6% of the Fe–Co sample and 38% of the Fe-only sample were reduced under the applied conditions, confirming that Co addition does not markedly promote Fe reduction.

In contrast, $FeCuK/ZrO_2$ exhibits distinct low-temperature reduction peaks at ~ 298 °C and ~ 350 °C, assigned to the reduction of $CuO \rightarrow Cu^0$ and $Fe_2O_3 \rightarrow Fe_3O_4$, respectively[33,38]. The presence of Cu promotes Fe reduction via a hydrogen spillover effect, resulting in higher overall H_2 consumption (~ 92% of theoretical) and a shift of Fe reduction to lower temperatures. A minor peak at ~ 450 °C corresponds to the further reduction of Fe_3O_4

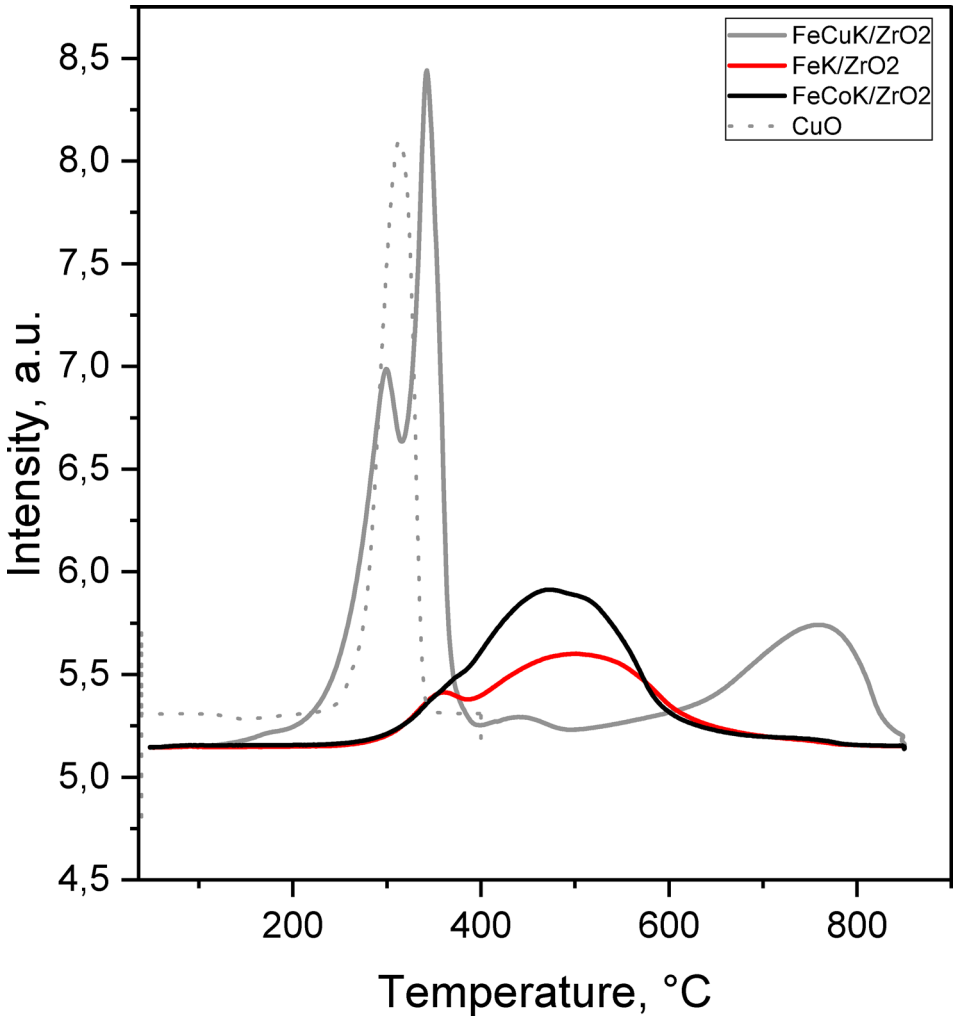

Fig. 4. H_2-TPR profiles of samples.

→ Fe, while a high-temperature signal at ~ 780 °C is attributed to Fe species strongly bound to the ZrO_2 lattice (Fe–O–Zr), which may coincide with partial ZrO_2 structural rearrangement from monoclinic to tetragonal.

For $FeCuK/ZrO_2$, the total theoretical H_2 consumption was 3055.4 μmol·g^{-1}, while the experimentally obtained value was 2804.2 μmol·g^{-1}, corresponding to ~ 92% overall reduction. Comparison of the reduction temperature of pure CuO ($T_{ne}d$ = 313 °C) with that of the bimetallic Cu–Fe sample ($T_{ne}d$ = 300 °C) reveals a slight shift to lower temperature, indicating a promoting effect of Cu on Fe reduction. The H_2 consumption between 150 and 400 °C was 1791.3 μmol·g^{-1}, exceeding the theoretical value expected for 2.3 wt% Cu alone, implying that roughly 50% of Fe species are reduced concurrently with Cu below 300 °C. An additional ~ 33% of Fe_2O_3 is reduced at temperatures above 350 °C, while the remaining ~ 20% requires higher temperatures (> 800 °C) for complete reduction.

Despite the enhanced reducibility of $FeCuK/ZrO_2$, its CO_2 hydrogenation activity is lower than that of FeK/ZrO_2 and $FeCoK/ZrO_2$. This can be attributed to the overly rapid reduction of Fe to metallic form in the presence of Cu, favoring the formation of highly dispersed Fe clusters that are less prone to controlled carburization into the active Fe_2C_5 phase. In contrast, the slower, higher-temperature reduction of Fe in FeK/ZrO_2 and $FeCoK/ZrO_2$ enables gradual Fe_2C_5 formation, which promotes hydrocarbon production. These findings highlight that optimal CO_2 hydrogenation performance requires not only sufficient Fe reducibility but also controlled reduction kinetics that favor the generation of the active carbide phase rather than rapid metallic Fe formation.

FTIR and Raman analysis – structural features of active sides

The FTIR spectra of catalysts (Fig. 1 – supporting information) show the characteristic peaks in the range 415–754 cm^{-1} corresponding to vibrational modes of Fe-O and Zr-O stretching bands[29,37]. The $FeCuK/ZrO_2$ and $FeCoK/ZrO_2$ catalysts exhibit Zr-OH stretching and hydroxyl group bending vibrations at 1360 and 1610 cm^{-1}, respectively, which may result from adsorption of H_2O[37–39]. For $FeCoK/ZrO_2$ we observed metal oxide vibrations at 1570 cm^{-1} close to typical OH-group bending vibrations. This sample also showed a broad peak positioned at 3420 cm^{-1}. This can be attributed to the hydroxyl group stretching vibration, caused by physisorption of water according to the work of Zhang et al.[40].

Raman spectroscopy is sensitive to metal–oxygen arrangements and lattice defects and was employed to obtain additional structural information. Raman spectra of the samples are shown in Fig. 5. Most characteristic peaks for all samples are centered at 183, 301, 335, 381, 476, 536, 559, 613, and 636 cm^{-1} for monoclinic ZrO_2[29]. These bands, present in all samples, clearly indicate that m-ZrO_2 is the dominant phase. For the FeCoK and FeCuK samples, additional peaks appearing at 149, 224, 292, 324, 407, 456 cm^{-1} refer to the existence of tetragonal ZrO_2[29]. Interestingly, these two samples exhibited a broad peak between 500 and 650 cm^{-1} related to disordered lattice oxygen along with mass-related disorder (stoichiometry imbalance). This can be explained by the insertion of Fe and Co(Cu) into ZrO_2 lattice[41,42]. Since the cations are much heavier than the oxygen atoms, they are the major contributors to the vibrations associated with the acoustic branches, indicating a periodic arrangement of the vacancies in Fe-Co(Cu) doped zirconia in the lattice. Specifically, distinct vibrational spectra have been well identified for both monoclinic and tetragonal zirconia. A pure phase of tetragonal zirconia is typically formed above 1205 °C; however, the tetragonal phase has been observed in zirconia grown over zirconium and zirconium alloy surfaces at lower temperatures[42]. This phenomenon has been discussed in the literature[42], where two different mechanisms for stabilizing the tetragonal ZrO_2 phase are proposed. Signals corresponding to these tetragonal phases, as well as bulk m-ZrO_2, can be observed in Fig. 5. In our case, the interaction of Fe and/or Co species with the ZrO_2 support—rather than confirmed alloy formation—may contribute to similar stabilization effects under the reaction conditions. This interpretation is based on analogy with the lattice-distortion mechanisms reported in[41,42], where atom-size mismatch and stoichiometric variations can influence the stabilization of the t-ZrO_2 phase. A careful examination of the Raman spectrum of the FeK sample shows weak bands around 263 cm^{-1}, consistent with Fe–Fe vibrations, while characteristic tetragonal ZrO_2 bands are not observed. This suggests that the dominant phases are m-ZrO_2 and Fe species in oxide form. The Raman spectrum of the FeCoK sample exhibits a feature at 715 cm^{-1}, commonly associated with Fe–Co interactions, which indicates that Fe–Co alloying is plausible but cannot be definitively established without complementary structural characterization.

Catalytic activity and stability

Table 3 summarizes the catalytic performance of Fe-based catalysts for light-olefin synthesis via CO_2 hydrogenation at 350 °C and 400 °C. Prior to testing, all catalysts were reduced in flowing H_2 at 400 °C for 4 h and evaluated under identical fixed-bed conditions.

An increase in reaction temperature from 350 °C to 400 °C led to higher CO_2 conversions for all catalysts. However, the corresponding temperature dependence yields apparent activation energies of only 4–26 kJ mol^{-1}, which are substantially lower than typical intrinsic barriers for the reverse water–gas shift (RWGS) or Fischer–Tropsch (FT) reactions (usually 60–120 kJ mol^{-1}). Such low values indicate that the overall process is partly constrained by thermodynamic equilibrium rather than by intrinsic kinetics, especially for catalysts dominated by RWGS[43–45]. Calculated RWGS equilibrium conversions under the present conditions (~ 30–40% at 350–400 °C, H_2/CO_2 = 3) closely match the experimental conversions, confirming that the system operates near equilibrium[46]. Therefore, the apparent activation energies most likely reflect network-averaged behavior rather than true kinetic barriers for a single elementary step[47].

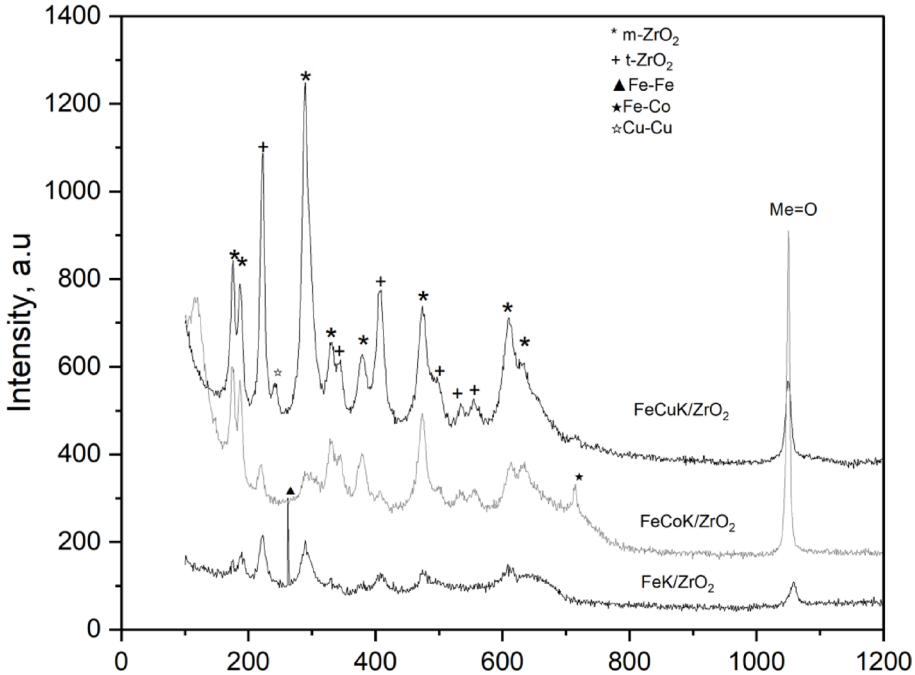

Fig. 5. Raman spectra of FeK/ZrO_2, FeCoK/ZrO_2, and FeCuK/ZrO_2.

Product distribution, %										
Catalysts	CO2 conversion	CO	CH4	C2-C4 paraffins	C2-C4 olefins	C5	C6	C7	other	C balance
350 °C										
FeK/ZrO2	32	30	14	8	28	6	7	4	4	101
FeCoK/ZrO2	36	28.5	14	5	28	7	2	5	9	98.5
FeCuK/ZrO2	30	40	10.3	4.3	17.3	5.5	5.5	5.4	13	101.3
400 °C										
FeK/ZrO2	43	25	22	6.6	28.4	6	5.4	4.3	2.6	100.3
FeCoK/ZrO2	38	26	23	5	30.3	6.4	2	3.2	4.4	98.3
FeCuK/ZrO2	39	28	15	7.3	22.3	4.5	5	3.5	10	95.6

Table 3. Conversion and product distribution in CO_2 hydrogenation at 350 and 400 °C.

At 350 °C, CO was the main product for all catalysts, consistent with RWGS dominance. Increasing temperature decreased CO selectivity while promoting hydrocarbon formation, indicative of RWGS–FT coupling. Despite not exhibiting the highest CO_2 conversion, FeCoK/ZrO_2 achieved the greatest C_2–C_4 olefin selectivity (≈ 30%) at 400 °C, suggesting that Co promotes chain propagation relative to methanation. Raman analysis revealed a band at ≈ 715 cm^{-1}, characteristic of Fe–Co mixing phase formation, which enhances H_2 activation and CO dissociation[48].

In contrast, FeCuK/ZrO_2 displayed the highest CO selectivity at 350 °C but the lowest olefin yield at 400 °C, attributed to the formation of FeO and Cu–Cu phases that hinder carburization and suppress FT chain growth[49]. Nevertheless, FeCuK/ZrO_2 most effectively limited CH_4 formation, suggesting that Cu favors CO desorption over further hydrogenation.

H_2-TPR analysis reveals that the reducibility of Fe species plays a decisive role in the formation of active phases and, consequently, in determining catalytic performance. In FeCuK/ZrO_2, most Fe species are reduced at relatively low temperatures (~ 298–350 °C) due to Cu-mediated hydrogen spillover, leading to rapid formation of metallic Fe. While this accelerates CO production and limits CH_4 formation, it suppresses the controlled carburization of Fe into the Fe_2C_5 phase, resulting in lower olefin yields. In contrast, FeK/ZrO_2 and FeCoK/ZrO_2 exhibit higher-temperature reduction (~ 500–510 °C) and a slower, stepwise Fe reduction pathway that allows Fe_3O_4 to remain stable under reaction conditions. This Fe_3O_4 phase functions both as an active site for CO_2 hydrogenation and as a precursor for gradual Fe_2C_5 formation, which promotes hydrocarbon chain growth and enhances C_2–C_4 olefin selectivity. Therefore, achieving an optimal balance between moderate Fe reducibility and controlled Fe_3O_4-to-Fe_2C_5 transformation is crucial for tuning the interplay between the reverse water–gas shift (RWGS) and Fischer–Tropsch (FT) steps. These results highlight that the rate of Fe reduction, rather than its extent alone, is a key determinant of both catalytic activity and product selectivity.

A complete carbon mole balance was applied to all products (CO, CH_4, C_2–C_4 hydrocarbons), ensuring data consistency and reliability.

Finally, the ZrO_2 polymorph appears to influence activity: catalysts supported on mixed monoclinic/tetragonal ZrO_2 exhibited higher CO_2 conversion and olefin selectivity, consistent with reports that tetragonal ZrO_2 enhances Fe dispersion and CO_2 adsorption strength, thereby facilitating RWGS–FT coupling[50]. Overall, the data demonstrate that the combination of a partially carburized Fe phase and Co promotion yields the most favorable balance between RWGS and FT steps, maximizing olefin selectivity under near-equilibrium conditions.

The stability tests of FeK/ZrO_2 and FeCoK/ZrO_2 at 400 °C and 30 bar for 60 h are presented in the supplementary information (Fig. 2 – supporting Information). Both catalysts maintain an almost constant CO_2 conversion throughout the entire time, indicating good structural integrity. However, both FeK/ZrO_2 and FeCoK/ZrO_2 catalysts show a gradual decrease in light olefin selectivity over time while maintaining stable performance. Nevertheless, the FeCoK sample after 20 h demonstrated stable olefin selectivity compared to other catalyst, which showed a further decrease in olefin selectivity.

The catalytic efficiency of Fe/ZrO_2 based systems, comparable in composition to our catalysts for the hydrogenation of CO_2 to light olefins is summarized in Table 4. In general, the activity and selectivity of the prepared catalysts fall within the range reported in the literature for similar Fe–ZrO_2 formulations[11,21,25,26,29,30,35]. The monometallic FeK/ZrO_2 catalyst exhibited a CO_2 conversion of 32% with moderate selectivity to light olefins (28%), confirming the promoting effect of potassium, which enhances catalyst basicity and facilitates the formation of Fe_5C_2 active phases while suppressing excessive methanation. The introduction of Cu (FeCuK/ZrO_2) led to a slight decrease in CO_2 conversion (30%) but a markedly higher CO selectivity (40%) and increased formation of heavier hydrocarbons (C_5–C_8 ≈ 17%), indicating that Cu promotes the reverse water–gas shift (RWGS) reaction and favors secondary chain-growth pathways. In contrast, the FeCoK/ZrO_2 catalyst achieved the highest CO_2 conversion (36%) with a comparable olefin selectivity (28%), suggesting a synergistic interaction between Fe and Co that enhances the reduction–carburization equilibrium and improves CO dissociation kinetics. Compared with previous studies, the present catalysts show competitive activity and olefin yields under relatively mild space velocities (6×10^3 mL g^{-1} h^{-1}), demonstrating efficient utilization of active Fe sites. These results confirm that appropriate promoter selection (K, Cu, or Co) can effectively tune the balance between RWGS and Fischer–Tropsch synthesis pathways, thereby directing the product distribution toward light olefins.

Catalyst	CO_2 Conv. (%)	CO Sel. (%)	CH_4 Sel. (%)	C_2–C_{4an} Sel. (%)	C_2–C_{4en} Sel. (%)	C_5–C_8 Sel. (%)	T (°C)	P (bar)	GHSV ($mL \cdot g^{-1} \cdot h^{-1}$)	Reference
FeK/ZrO_2	32	30	14	8	28	18	350	30	6	Our work
FeCuK/ZrO_2	30	40	10.3	5	17	17	350	30	6	Our work
FeCoK/ZrO_2	36	28	14	5	28	13	350	30	6	Our work
Fe–ZrO_2 + K	36	20	15	10	30	5	350	20	12	11
FeK/ZrO_2	30	18	10	12	50	–	320	2	9	25
Fe/ZrO_2	25	10	20	8	35	–	340	10	10	30
FeOx/ZrO_2	37	25	14	15	40	6	340	10	15	29
Fe_2O_3/ZrO_2	18	35	40	10	12	–	300	1	6	35
Fe/ZrO_2	40	22	20	10	38	5	350	20	8	21

Table 4. CO_2 hydrogenation to light olefins over Fe/ZrO_2-based catalysts – comparison with literature. !Reaction conditions and selectivity values are those corresponding to optimal light olefin yields reported in each study. "–" indicates data not reported. C_2–C_4an = paraffins; C_2–C_4en = olefins.

Conclusion

The comprehensive characterization of the Fe-based catalysts supported on ZrO_2, including N_2 physisorption, XRD, TEM, H_2-TPR, and Raman spectroscopy, reveals important insights into the structure, morphology, and reducibility of the materials, which directly correlate with their catalytic performance in CO_2 hydrogenation.

The N_2 adsorption-desorption isotherms and pore size distributions indicate that the metal loading affects the textural properties of the catalysts. Specifically, the introduction of Fe, Co, and Cu leads to a decrease in surface area and pore volume, with FeCuK/ZrO_2 showing the most significant structural densification due to Cu-induced sintering. Despite these changes, the mesoporous framework of ZrO_2 is preserved, indicating that the catalysts maintain their porous structure after metal loading.

XRD analysis confirmed the successful incorporation of the metal species, with the FeK/ZrO_2 and FeCoK/ZrO_2 catalysts showing good metal dispersion and Fe reduction to metallic α-Fe. In contrast, FeCuK/ZrO_2 exhibited larger crystalline Cu particles, suggesting that Cu induces sintering or agglomeration of metal species, which could negatively impact catalytic performance. The reducibility of the catalysts, as assessed by H_2-TPR, revealed that Cu enhances Fe reducibility through hydrogen spillover, leading to lower reduction temperatures compared to FeK/ZrO_2 and FeCoK/ZrO_2, where Co plays a role in modifying the Fe–ZrO_2 interface, creating oxygen vacancies, and altering the reducibility of Fe.

Overall, the combined textural, structural, and reducibility data provide a clear link between the physical characteristics of the catalysts and their CO_2 hydrogenation activity. The FeK/ZrO_2 and FeCoK/ZrO_2 catalysts showed promising performance due to their well-dispersed metal phases and enhanced reducibility, with FeCoK/ZrO_2 emerging as the most active catalyst for light olefin synthesis. In contrast, the FeCuK/ZrO_2 catalyst exhibited a reduced CO_2 conversion rate due to the poorer metal dispersion and reduced active site density caused by Cu-induced sintering. These findings emphasize the importance of careful metal promoter selection and the optimization of metal dispersion for achieving high catalytic performance in CO_2 hydrogenation reactions.

Methods

Catalyst Preparation and characterization

Catalyst Preparation

Chemicals and materials: $Fe(NO_3)_3 \cdot 9H_2O$, $Cu(NO_3)_2 \cdot 3H_2O$, $Co(NO_3)_2 \cdot 6H_2O$, K_2CO_3 from Sigma-Aldrich and commercial m-ZrO_2 from DK-Japan.

Preparation: ZrO_2-supported FeK or Fe(M) K, where M is Co, Cu, catalysts were prepared by wet impregnation method. Content of Fe in samples is 10 wt% and molar ratio M/(Fe + M) = 0.17. The amount of K was 1.3 wt% in all samples. The catalysts were dried at 120 °C overnight and calcined at 500 °C for 4 h.

Physical-chemical characterization

The specific surface area (S_{BET}) and porosity of the materials were calculated from the nitrogen adsorption-desorption isotherms recorded at −196 °C with a BELSORP-mini II (BEL Japan, Inc.) surface area and pore size analyzer. Prior to measurements, the samples were outgassed for 2 h at 250 °C. S_{BET} was calculated using the Brunauer-Emmet-Teller (BET) equation for the N_2 relative pressure range of $0.05 < p/p_0 < 0.30$. Pore size distribution was determined by the Barrett-Joyner-Halenda (BJH) method from the desorption branch of the isotherm.

XRD powder patterns were recorded on a Panalytical X'Pert θ/2θ-diffractometer equipped with Xcelerator detector using automatic divergence slits and Cu Kα1/α2 radiation (40 kV, 40 mA; λ = 0.15406 nm, 0.154443 nm). Cu beta-radiation was excluded using a nickel filter foil. The measurements were performed at 0.021–0.005 s^{-1}, respectively. Samples were mounted on silicon zero background holders. Obtained intensities were converted from automatic to fixed divergence slits (0.25) for further analysis. X-ray diffraction (XRD) patterns for reduced samples was made with Mo Kα radiation (λ = 0.07093 nm). The use of Mo radiation for the reduced, Fe-containing samples effectively suppresses fluorescence from metallic Fe and provides improved diffraction quality for dense or metallic phases.

Temperature-programmed reduction (TPR) measurements were performed in a 3-Flex apparatus (Micromeritics) with quartz tube reactor and thermal conductivity detector for quantification. Around 100 mg of sample was loaded into the reactor and pretreated at 400 °C (20 K/min) under Ar flow for 30 min and cooled to RT. Then, flow was changed to 50 ml/min H_2/Ar and the temperature was ramped to 900 °C at a heating rate of 10 K/min and held for 30 min. The H_2 consumption peaks were recorded with temperature and the peak areas were quantified using experimental calibration factors. Based on the stoichiometric reduction reactions, the theoretical hydrogen consumption was calculated to be 2688.2 μmol $H_2 \cdot g^{-1}$ for a sample containing 10 wt% Fe and 367.2 μmol $H_2 \cdot g^{-1}$ for a sample containing 2.3 wt% Cu.

FT-IR ATR spectra were acquired through a VERTEX 70 V Bruker spectrophotometer equipped with a platinum ATR unit with diamond crystal (η = 2.4) operating in the spectral range between 4000 and 400 cm^{-1} at a spectral resolution of 2 cm^{-1} and with 120 scans. Spectra were acquired at a pressure of 2 hPa. In all spectra, a baseline correction of scattering was made. Data analysis was performed using the OPUS 7.5® software.

Raman spectra were recorded using an XploRA Plus micro spectrometer (Horiba Scientific, Kyoto, Japan), equipped with a laser emitting at 638 nm. The acquisition time was set to 50 s and all the measurements were performed at room temperature using a 50X long working distance microscope objective (Evident corporation-Olympus, Tokyo, Japan), which helped to focus the laser beam contactless on the sample surface. Raman signal was collected in a backscattered configuration through the same objective and was subsequently dispersed by a diffraction grating (1800 lines/mm) onto a CCD detector (Syncerity, Horiba Scientific).

TEM micrographs were acquired using a Jeol JEM-F200 cold-FEG S/TEM at a voltage of 200 kV. The samples were ground to fine powder and then suspended in ethanol. One drop of this suspension was put on a holey-carbon-coated copper grid of 300 mesh and left in air to dry.

Catalytic test

The samples were tested in CO_2 hydrogenation in a fixed-bed reactor. The reactor temperature was measured with a type K thermocouple positioned in the catalyst bed. The reactor was mounted in a furnace equipped with a PID temperature controller. All downstream lines were kept at 180 °C. The gas flow rates were controlled with Bronkhorst mass flow controllers. The calcined catalyst (200 mg, 0.2–0.4 mm fraction) was diluted with inert SiO_2 (approx. 2.0 g, 0.3–0.4 mm particle size) to avoid hot spots. Before exposing to reaction conditions, the as-prepared catalysts were activated in situ with H_2 (20 ml/min) at 400 °C for 4 h. Reaction conditions for the hydrogenation of CO_2 to light olefins were fixed as follows: $CO_2/H_2/N_2$ ratio in the feed = 1:3:1; pressure = 30 bar, temperature set points = 400 – 350–300 °C and GHSV = 6000 $ml \cdot h^{-1} \cdot g^{-1}$. The processing time for each test was 15 h. A stability test with run time of more than 60 h was made for the most active catalysts. CO_2 conversion and product selectivity were calculated as follows:

$$\boldsymbol{X}\,(\boldsymbol{CO_2}) = 1 - \frac{\dot{\boldsymbol{n}}_{\boldsymbol{CO_2}}^{\boldsymbol{out}}}{\dot{\boldsymbol{n}}_{\boldsymbol{CO_2}}^{\boldsymbol{in}}} \qquad\qquad \boldsymbol{S_i} = \frac{\boldsymbol{a_i}\dot{\boldsymbol{n}}_{\boldsymbol{i}}^{\boldsymbol{out}}}{\sum_{\boldsymbol{j=1}}^{\boldsymbol{n}} \boldsymbol{a_j}\dot{\boldsymbol{n}}_{\boldsymbol{j}}^{\boldsymbol{out}}}$$

Whereby $\dot{\boldsymbol{n}}_{\boldsymbol{i}}^{\boldsymbol{out}}$ and $\dot{\boldsymbol{n}}_{\boldsymbol{i}}^{\boldsymbol{in}}$ are the molar streams of the i-component at the reactor inlet and outlet. $\boldsymbol{a_i}$ = carbon number of the i-component.

Data availability

All data generated or analysed during this study are included in this published article.

Received: 11 August 2025; Accepted: 30 December 2025
Published online: 16 January 2026

References

1. More, A. *Light Olefins Market Size 2020 Industry Share, Trends Evaluation, Global Growth, Recent Developments, Latest Technology, and 2025 Future Forecast Research Report (n.d.); 2021*.
2. Gnanamani, M. K. et al. Hydrogenation of carbon dioxide over Co–Fe bimetallic catalysts. *ACS Catal.* **6**, 913–927 (2016).
3. Yang, H. et al. A review of the catalytic hydrogenation of carbon dioxide into value-added hydrocarbons. *Catal. Sci. Technol.* **7**, 4580–4598 (2017).
4. Wang, D. et al. Recent advances in carbon dioxide hydrogenation to produce olefins and aromatics. *Chem* **7**, 2277–2311 (2021).
5. Liu, J. et al. Recent advances in application of ironbased catalysts for COx hydrogenation to value-added hydrocarbons. *Chin. J. Catal.* **43**, 731–754 (2022).
6. Visconti, C. G. et al. CO2 hydrogenation to hydrocarbons over Co and Fe-based Fischer-Tropsch catalysts. *Catal. Today*. **277**, 161–170 (2016).
7. Fan, T. et al. Cobalt catalysts enable selective hydrogenation of CO2 toward diverse products: recent progress and perspective. *J. Phys. Chem. Lett.* **12**, 10486–10496 (2021).
8. Satthawong, R. et al. Bimetallic Fe-Co catalysts for CO2 hydrogenation to higher hydrocarbons. *J. CO2 Util.* **3**, 102–106 (2013).
9. Bahari, M. B. et al. A short review on bimetallic Co-based catalysts for carbon dioxide reforming of methane. *Mater. Today*. **42**, 94–100 (2021).
10. Zhu, M. & Wachs, I. E. Iron-based catalysts for the high-temperature water-gas shift (HT-WGS) reaction: a review. *ACS Catal.* **6**, 722–732 (2016).
11. lan Barrios, D. P. et al. Efficient promoters and reaction paths in the CO 2 hydrogenation to light olefins over ZirconiaSupported iron catalysts. *ACS Catal.* **12** (5), 3211–3225 (2022).
12. Ge, Y., Martín, Z. T. & Pérez-Ramírez, A. J. ZrO2-Promoted Cu-Co, Cu-Fe and Co-Fe catalysts for higher alcohol synthesis. *ACS Catal.* **13** (15), 9946–9959 (2023).
13. Jiang, Y. et al. Recent advances in thermocatalytic hydrogenation of carbon dioxide to light olefins and liquid fuels via modified Fischer-Tropsch pathway. *J. CO2 Util.* **67**, 102321 (2023).
14. Sato, A. G. et al. Effect of the ZrO2 phase on the structure and behavior of supported Cu catalysts for ethanol conversion. *J. Catal.* **307**, 1–17 (2013).

15. Vourros, A. et al. Carbon dioxide hydrogenation over supported Au nanoparticles: effect of the support. *J. CO2 Utal.* **19**, 247–256 (2017).
16. Prieto, G. et al. Towards stable catalysts by controlling collective properties of supported metal nanoparticles. *Nat. Mater.* **12**, 34–39 (2013).
17. Kattel, S. et al. CO2 hydrogenation over oxide-supported PtCo catalysts: the role of the oxide support in determining the product selectivity. *Angew Chem. Int. Ed.* **55**, 7968–7973 (2016).
18. Kattel, S. et al. Optimizing binding energies of key intermediates for CO2 hydrogenation to methanol over oxide-supported copper. *J. Am. Chem. Soc.* **138**, 12440–12450 (2016).
19. Dou, M. et al. Theoretical study of methanol synthesis from CO2 and CO hydrogenation on the surface of ZrO2 supported In2O3 catalyst. *Surf. Sci.* **672–673**, 7–12 (2018).
20. Wang, G. et al. Methanol synthesis from CO2 hydrogenation over CuO-ZnO-ZrO2-MxOy catalysts (M = Cr, mo and W). *Intern. J. Hydrogen Energy*. **44**, 4197–4207 (2019).
21. Al-Dossary, M. & Fierro, J. L. G. Effect of high-temperature pre-reduction in Fischer–Tropsch synthesis on Fe/ZrO2 catalysts. *Appl. Catal. A*. **499**, 109–117 (2015).
22. Ting, K. W. et al. Low-Temperature hydrogenation of CO2 to methanol over heterogeneous TiO2-Supported re catalysts. *ACS Catal.* **9**, 3685–3693 (2019).
23. Jun, K. W. et al. Support effects of the promoted and unpromoted iron catalysts in CO2 hydrogenation. *Stud. Surf. Sci. Catal.* **114**, 345–350 (1998).
24. Wang, Y. H. et al. Structure-activity relationships of Cu-ZrO2 catalysts for CO2 hydrogenation to methanol: interaction effects and reaction mechanism. *RSC Adv.* **7**, 8709–8717 (2017).
25. Gu, H. et al. Promotion of surface oxygen vacancies on the light olefins synthesis from catalytic CO2 hydrogenation over FeK/ZrO2 catalysts. *Int. J. Hydrog. Energy*. **44** (23), 11808–11816 (2019).
26. Wang, W. et al. Fe – Cu bimetallic catalysts for selective CO2 hydrogenation to Olefin-Rich C2 + Hydrocarbons. *Ind. Eng. Chem. Res.* **57**, 4535–4542 (2018).
27. Fiordaliso, E. M. et al. Intermetallic gapd nanoparticles on SiO2 for low-pressure CO2 hydrogenation to methanol: catalytic performance and in situ characterization. *ACS Catal.* **5**, 5827–5836 (2015).
28. Pandey, D. & Deo, G. Promotional effects in alumina and silica supported bimetallic Ni-Fe catalysts during CO2 hydrogenation. *J. Mol. Catal. A: Chem.* **382**, 23–30 (2014).
29. Zhao, Q. et al. Crucial role of surface FeOx components on supported Fe-Based nanocatalysts for CO2 hydrogenation to light olefins. *Ind. Eng. Chem. Res.* **62**, 9420–9432 (2023).
30. Huang, J. et al. Dynamic evolution of Fe and carbon species over different ZrO2 supports during CO prereduction and their effects on CO2 hydrogenation to light olefins. *ACS Sustain. Chem. Eng.* **9** (23), 7891–7903 (2021).
31. Li, K. & Chen, J. G. CO2 hydrogenation to methanol over ZrO2-Containing catalysts: insights into ZrO2 induced synergy. *ACS Catal.* **9**, 7840–7861 (2019).
32. Dong et al. Nanocomposites of reduced graphene oxide with pure monoclinic-ZrO2 and pure tetragonal-ZrO2 for selective adsorptive removal of Oxytetracycline. *Appl. Surf. Sci.* **543**, 148810 (2021).
33. Wang, J. et al. Synthesis of lower olefins by hydrogenation of carbon dioxide over supported iron catalysts. *Catal. Today*. **215**, 186–193 (2013).
34. Chernavskii, P. A. et al. Influence of copper and potassium on the structure and carbidisation of supported iron catalysts for Fischer–Tropsch synthesis. *Catal. Sci. Technol.* **7** (11), 2325–2334 (2017).
35. Chen, K. et al. Carbon monoxide hydrogenation on Fe2O3/ZrO2 catalysts. *Catal. Lett.* **36** (3), 139–144 (1996).
36. Li, W. et al. A short review of recent advances in CO2 hydrogenation to hydrocarbons over heterogeneous catalysts. *RSC Adv.* **8** (14), 7651–7669 (2018).
37. Gao, X. et al. Reduction of supported iron oxide studied by temperature-programmed reduction combined with mössbauer spectroscopy and X-ray diffraction. *J. Chem. Soc., Faraday Trans.* **89** (7), 1079–1084 (1993).
38. Jozwiak, W. K., Maniecki, E. K. T. P., Ignaczak, W. & Maniukiewicz, W. Reduction behavior of iron oxides in hydrogen and carbon monoxide atmospheres. *Appl. Catal. A*. **326**, 17–27 (2007).
39. Ding, J. et al. *CO2 hydrogenation to light olefins with high-performance Fe0.30Co0.15Zr0.45K0.10O1.63.* Journal of Catalysis, 377: pp. 224–232. (2019).
40. Zhang, Y. et al. Controlled Synthesis, Characterization, and Morphology-Dependent reducibility of Ceria – Zirconia – Yttria solid solutions with Nanorod-like, Microspherical, Microbowknot-like, and Micro-octahedral shapes. *Inorg. Chem.* **48** (5), 2181–2192 (2009).
41. Corey, M. et al. Characterization of zirconium oxides part I: Raman mapping and spectral feature analysis. *Nuclear Mater. Energy*. **21**, 100707 (2019).
42. Efaw, C. M. et al. Characterization of zirconium oxides part I: Raman mapping and spectral feature analysis. *Nuclear Mater. Energy*. **21**, 100707 (2019).
43. Ting, C., Lin, E. E. B. R. & Bhan, A. Kinetic and thermodynamic considerations in thermocatalytic CO2 hydrogenation. *ACS Catal.* **14**, 9261–9275 (2024).
44. Owen, R. E. Kinetics of CO2 hydrogenation to hydrocarbons over Iron–Silica catalysts. *ChemPhysChem* **18**, 3219–3230 (2017).
45. Kesha, N. et al. Intermediate-Temperature reverse Water–Gas shift under Process-Relevant conditions catalyzed by dispersed alkali carbonates. *JACS Au*. **5**, 1071–1083 (2025).
46. Changjian Zhou, C. Z., Zhang, J. & Fu, Y. Hui Dai *Recent advances in the reverse Water–Gas conversion reaction*. *Molecules* **28**, 7657 (2023).
47. Krausser, L. et al. Formation and role of Iron-Containing phases in CO2 hydrogenation to higher hydrocarbons. *ACS Catal.* **15**, 10627–10638 (2025).
48. Jie Zhu, P. W. et al. Dynamic structural evolution of iron catalysts involving competitive oxidation and carburization during CO2 hydrogenation. *Sci. Adv.* **8**(5), 3629 (2022).
49. Jofrey, J., Masana, B. P., Shuai, Z., Qiu, M. & Yu, Y. Influence of halide ions on the electrochemical reduction of carbon dioxide over a copper surface. *J. Mater. Chem. A*. **10**, 1086–1104 (2022).
50. Zichittella, G. et al. Halogen-Dependent surface confinement governs selective alkane functionalization to olefins. *Angew Chem. Int. Ed.* **58**, 5877 (2019).

Acknowledgements

Funding by BMWi (FKZ 03EE5060B) is gratefully acknowledged.

Author contributions

E.K. conceived the study and designed the methodology.U.A. supervised the writing process and planned the experiments.C.G. performed the TEM investigation.R.C.P. conducted the Raman investigation.M.L.S. carried out the FT-IR investigation.The manuscript was prepared with contributions from all authors. All authors reviewed and approved the final version of the manuscript.

Funding
Funding by BMWi (FKZ 03EE5060B) is gratefully acknowledged.

Declarations

Competing interests
The authors declare no competing interests.

Additional information
Supplementary Information The online version contains supplementary material available at https://doi.org/10.1038/s41598-025-34708-7.

Correspondence and requests for materials should be addressed to E.K.

Reprints and permissions information is available at www.nature.com/reprints.

Publisher's note Springer Nature remains neutral with regard to jurisdictional claims in published maps and institutional affiliations.